Enhanced dust emission following large wildfires due to vegetation disturbance

Yan Yu[1,2*] and Paul Ginoux[3]

[1]Department of Atmospheric and Oceanic Sciences, School of Physics, Peking University, Beijing, China
[2]Laboratory for Climate and Ocean-Atmosphere Studies, Department of Atmospheric and Oceanic Sciences, School of Physics, Peking University, Beijing, China
[3]NOAA Geophysical Fluid Dynamics Laboratory, Princeton, NJ, USA
*Correspondence to Yan Yu (yuyan@pku.edu.cn)

Abstract

Large wildfires reduce vegetation cover and soil moisture, leaving the temporally degraded landscapes an emergent source of dust emission. However, the global extent of post-fire dust events and their influencing factors remain unexplored. Using satellite measurements of active fires, aerosol abundance, vegetation cover and soil moisture from 2003 to 2020, here we show that 54% of the examined ~150,000 global large wildfires are followed by enhanced dust emission, producing significant dust loadings for days to weeks over normally dust-free regions. The occurrence and duration of post-fire dust emission is primarily controlled by the extent of precedent wildfires and resultant vegetation anomalies, and secondarily modulated by pre-fire drought conditions. The intensifying wildfires and drying soils during the studying period have made post-fire dust events one day longer, especially over extratropical forests and grasslands. With the predicted intensification of regional wildfires and concurrent droughts in the upcoming decades, our results indicate a future enhancement of sequential fire and dust extremes and their societal and ecological impacts.

Main

Wildfires represent a major ecosystem disturbance and aerosol emission source, affecting the global carbon budget, climate, and human life[1,2]. Short-term influences of wildfires include damaged infrastructures, degraded air quality, and nutrient redistribution caused by the emission of smoke aerosols[3,4]. In situ and remote sensing measurements have also suggested the presence of mineral dust in smoke plumes[3,5], caused by pyroconvective updraft from nearby burning[6]. Longer-term influences of wildfires primarily involve vegetation disturbances and resultant changes in ecosystem, hydroclimate, and geomorphology[7,8]. Among the natural consequences of the destroyed vegetation, especially the short species such as grasses and shrubs[8], is the expansion of bare ground that is particularly susceptible to wind erosion[9]—the detachment of soil particles from the ground, and dust storms in an extreme condition[10]. The intensity of wind erosion and resultant dust emission depends on wind friction velocity[11], vegetation structure[12], and soil properties[10]. In addition to the clearance of vegetation and biocrusts cover, several additional features of wildfires may exacerbate the occurrence of post-fire dust storms. First, the fire-induced reduction in vegetation leads to an expanded vegetation canopy gap and reduced vegetation height, aerodynamically intensifying the severity of wind erosion[12]. Second, large wildfires are often associated with climate-driven, dry fuels and accompanying dry soils[13], which favor dust emission. Moreover, fires may alter the physical and chemical properties of soils and disrupt the wet-bonding forces[14], thereby further promoting the occurrence of wind erosion from these burned landscapes.

In situ observations and modeling studies have confirmed dust emission from post-fire landscapes mostly in North America[5,15–17]; yet, post-fire dust emission has not yet been globally examined using observational data. To fill this knowledge gap, the current study aims to (1) identify global hotspots of post-fire dust emission from a suite of satellite observations, (2) test the hypothesized driving mechanisms of dust emission after wildfires with observational data sets, and (3) diagnose the observed recent trends in the intensity and duration of post-fire dust emission.

Here we analyze a spectrum of satellite measurements of active fires, aerosol abundance and characteristics, vegetation cover, and soil moisture, as well as reanalysis wind for the period

2003–2020. This collection of global observational data sets well captures the dust emissions after wildfires during the 2010 and 2012 burning seasons in western United States, as reported by previous in situ observations and modeling studies[15,16] (**Extended Data Fig. 1**). Based on these observational datasets, we first identify large fire events with more than 20 active fires occurring within each 10 km pixel in consecutive seven day, and then search for significant vegetation reduction and accompanying enhanced dust load during the subsequent 60 days since the end of each large fire event (see Methods). To demonstrate the capability of currently applied satellite measurements in charactering post-fire dust events, we first show extreme dust emission from the burned areas during the 2019–2020 Australian bushfires. Statistical assessments of post-fire dust events across the entire globe are shown afterwards.

Dust emission after 2019–2020 Australian bushfires

Following the long-lasting drought conditions[18], a series of large wildfires burned a historic 186,000 km^2 across eastern Australia during the 2019–2020 bushfire season[19]. Satellite observations indicate a record-breaking low vegetation cover [represented by extremely low Enhanced Vegetation Index (EVI), a semi-quantitative measurement for the amount of vegetation, **Figure 1c**] and high dust concentration [represented by extremely high Dust Optical Depth (DOD), an approximate measure of columnar dust mass, **Figure 1d** and Supplementary **Fig. 1**] across the burned regions during December 2019 to February 2020. Indeed, the 2019–2020 bushfire season receives more than doubled dust loading, compared with an average year during the past two decades for this region[20]. Such a massive amount of dust particles is mainly emitted from the burned regions that witness the most severe vegetation damage. For example, the savannahs (around 27.8˚S, 152.3˚E) to the west of Brisbane experience a substantial reduction in vegetation cover (EVI drops from about 0.25 to 0.17, compared with a long-term average of 0.35) after the extensive fires during November 7–13, 2019 (**Figure 1b**). Following the persistent vegetation disturbances and abnormally dry soils, extreme DOD episodes are observed in December 2019 (**Figure 1a, b**). These post-fire dust episodes in eastern Australia are also captured by spaceborne lidar (Cloud-Aerosol Lidar with Orthogonal Polarization, CALIOP) measurements of total backscatter and depolarization ratio, as well as derived aerosol type information (**Extended Data Fig. 2**).

Global occurrence of post-fire dust emission

Based on the analyzed satellite measurements of fire, vegetation, and aerosols during the 18 years of 2003–2020 (see Methods), we identify 151,727 large wildfire events with more than 20 active fires detected in a 0.1˚ × 0.1˚ pixel during consecutive seven days. Among the analyzed large fire events, 91% and 54% are followed by significant EVI reduction and consequent dust events, respectively, during the subsequent 60 days. These 87,400 post-fire dust emission events are distributed across 36,386 0.1˚ pixels in the fire-prone regions of tropical savannahs in Africa, South America, and northern and eastern Australia, shrublands in western Australia, grasslands and croplands in central Asia, and various landscapes in western North America (**Figure 2a**). Among different landscapes, global savannahs contribute 66% of the currently identified large fire events, 59% of consequent significant EVI reduction, and 51% of post-fire dust events (**Figure 2b**).

The post-fire dust events typically last for 1–25 days and the maximum DOD ranges between 0.2 to 1.8 (**Figure 2c**); the intensity and duration of post-fire dust events vary by land cover type (**Figure 2d**). The post-fire maximum DODs are on average 351% (192% –578%, 10^{th}– 90^{th} percentiles of the relative increment among all pixels) larger than the local average DOD. Global savannahs see the most intensive (average DOD of 0.62, and 10^{th} – 90^{th} percentiles of 0.21–1.56) and long-lasting (median duration of 3.5 days, and 10^{th}–90^{th} percentiles of 1–10 days) post-fire dust events, compared with other landscapes (**Figure 2d**). Regionally, the most severe and long-lasting post-fire dust events are observed over savannahs in West Africa and tropical Africa to the north and south of the Congo rainforest, where maximum DOD after large fires reaches 1.8, about three folds of the local 95^{th} percentile of monthly DOD and close to that over the global leading dust sources, such as the Bodélé Depression in Chad[21,22] (**Extended Data Fig. 3b**). Moreover, the moderate-to-high DODs above 0.5 are widely seen over the normally dust-free regions, such as the boreal regions in North America and eastern Asia and mid-to-high latitudes in the Southern Hemispheric (**Figure 2c**). Indeed, among the 36,386 pixels where post-fire dust emissions are identified here, only 8% have ever experienced a DOD exceeding 0.2 that cannot be attributed to antecedent large wildfires during the study years.

Post-fire dust events occur episodically during weeks after large fires, due to the long-lasting, pre-fire dry soils and post-fire vegetation disturbances (**Extended Data Fig. 4**). The currently examined large wildfires cause a reduction in vegetation, represented by a shift in the probability distribution towards lower EVI during the first week after burning; this vegetation disturbance typically lasts for several months, accompanied by persistent dry soils (**Extended Data Figure 4b, c**). Corresponding to the anomalies in vegetation and soil moisture, the probability distribution of DOD shifts toward higher values, with the probability of DOD exceeding the long-term 90th percentile between 21% to 40% during the first eight weeks after large wildfires (**Extended Data Figure 4a**). Unlike the long-lasting EVI and soil moisture anomalies, elevated surface wind speed mainly occurs during the extensive wildfire events and decays afterwards (**Extended Data Fig. 4d**).

The occurrence and duration of post-fire dust emission largely depends on the temporal and spatial extent of precedent wildfires (**Figure 3**). As the extent of wildfires increases, the posterior vegetation cover lowers, weakening its physical protecting and aerodynamical sheltering effects on soils. Consequently, the probability of less vegetation, more dusty situations elevate after the occurrence of large wildfires, and further enhances with the increment of precedent fire counts (**Figure 3a**). Specifically, the probability of extremely low monthly EVI (lower than long-term 10th percentile) increases from 39% after a moderate fire event (with the occurrence of 21–30 fires) to 78% after a severe fire event (with more than 100 fires). The intensified precedent fires are also accompanied by generally lower soil moisture (**Extended Data Fig 5a**), either due to large-scale climate variations that favor dryer conditions for burning or due to fire-induced soil moisture depletion, which further favors dust emission. As a result, the probability of extremely high monthly DOD (exceeding the long-term 90th percentile) increases from 28% after a moderate fire event to 84% after a severe fire event (**Figure 3a**); and the median duration of post-fire dust events increases from one day (10th – 90th percentiles of 1–6 days) after a moderate fire event to 10 days (10th – 90th percentiles of 8–16 days) after a severe fire event (**Figure 3b**). Corresponding to this dependence of post-fire dust emission on the extent of burning, the seasonal peak of post-fire dust emission occurs simultaneously with or shortly after the seasonal peak of active fires across the majority of global post-fire dust emission hotspots (**Extended Data Fig. 6**).

The long-lasting (>5 days) post-fire dust events are mainly present over all land cover types when post-fire EVI falls below 0.20 (**Figure 3b and Extended Data Fig. 7**), a typical EVI value over the active arid and semi-arid dust sources, such as the Sahara Desert (**Extended Data Fig. 3a**). This relationship between post-fire EVI and post-fire dust event duration could serve as the basis for early warning of extreme post-fire dust activity. Noticeably, a large portion of the long-lasting post-fire dust events occur after a moderate fire event (**Figure 3b**). These long-lasting post-fire dust events after moderate fires are mostly observed over savannahs, mainly in Africa (**Extended Data Fig. 7c**), where transported dust from nearby dust sources[21] (e.g. Sahara, Sahel, and Middle East) are likely mixed with locally emitted dust from burned areas, thereby obscuring the accurate duration of these post-fire dust events.

The occurrence and intensity of post-fire dust events is also modulated by pre-fire drought conditions, as represented by soil moisture anomalies before the occurrence of fires (**Extended Data Figs. 8 and 9**). Over the semi-arid regions included in this analysis, drought conditions are favorable for dust emission from the sub-grid bare-soil areas, as reflected by the probability distribution of DOD towards higher values during dry periods even without fires, compared with wet periods (**Extended Data Fig. 8**). This difference in DOD probability distribution between relatively wet and dry periods partially diminishes after fires, indicating the primary role of fires on determining the occurrence and severity of post-fire dust events (**Extended Data Fig. 8**). Nevertheless, pre-fire drought conditions favor elevated occurrence and intensity of post-fire dust events (**Extended Data Fig. 9**).

Recent trends in post-fire dust emissions

While forest ecoregions have experienced a positive trend of 87.6 cases per decade in post-fire dust emission events (**Figure 4a**), other ecoregions have exhibited minimal changes in occurrence. However, the duration of these events has been increasing significantly (all p-values < 0.05, based on the Mann-Kendall monotonic trend test) over all landscapes, with a positive trend of 0.82, 0.54, 0.28, 1.05, and 0.80 days per decade over forests, shrublands, savannahs, grasslands, and croplands during 2003–2020 (**Figure 4b**). Indeed, the most long-lasting dust emission events are widely seen in either 2019 or 2020 over 4,699 pixels out of the 36,386 examined pixels (**Figure 4c**), such as those during the 2019–2020 Australian bushfire season (**Figure 1**) and 2020 western United States extreme fire season (**Extended Data Fig. 10**). This recent elongation of post-fire dust emission is attributed here to the increased extent of wildfires, as indicated by the positive trends in active fire counts (**Figure 4b**). For the forest, shrubland, savannah, grassland, and cropland pixels examined here, the averaged fire counts per 0.1° pixel per event increase by 3.50, 0.56, 0.37, 1.12, and 0.24 per decade, respectively, with all p-values < 0.05 except for the croplands, according to the Mann-Kendall test. Meanwhile, the analyzed forest, grassland, and cropland pixels exhibit moderately significant reduction ($p < 0.1$, based on the Mann-Kendall test) in pre-fire soil moisture during 2003 to 2020.

Discussion

Our findings have direct implications on the ecological and societal impacts of intensifying droughts and wildfires over certain landscapes. In addition to the instantaneous societal disruptions and health risks, drought and resultant wildfires set the stage for dust storms even weeks after burning. Our findings are further supported by recent in-situ observations[23] reporting that wildfires reduce soil biocrusts by 50%, which may also enhance dust emissions[24]. These post-fire dust storms could be as intensive as those observed in arid to semi-arid lands (**Figure 2** and **Extended Data Fig. 3b**) and cause similar infrastructure damages and air quality declines[25]. Compared with the dryland dust storms, the post-fire dust storms may cause even larger socioeconomic and health impacts, due to their closer location to populated areas and possible mixing of harmful combustion residuals into the post-fire dust storms. The emitted soil particles from these disturbed lands may enter the global dust cycle, altering the radiation budget[26], cloud and precipitation patterns[27], as well as oceanic[3] and terrestrial biogeochemistry[28]. For example, dust particles from Australia are key suppliers of iron, a bio-essential trace metal, to the iron-limited ecosystems of Southern Ocean. The recently uncovered widespread phytoplankton blooms from December 2019 to March 2020 in the Southern Ocean downwind of Australia[29] could be a result of the post-fire dust emission triggered by the 2019-2020 Australian bushfires (**Figure 1**, **Extended Data Fig. 2**, and **Supplementary Fig. 1**). On the other hand, the high-latitude post-fire dust emissions (**Figure 2a, c**) may provide an additional source for light-absorbing aerosols, beyond transported dust and smoke, that may accelerate snow darkening and melting with warming[30]. Furthermore, the currently identified role of drought and fires on post-fire dust emission (**Figure 3**, **Extended Data Figs. 8** and **9**) will potentially become more interactive and complicated in the upcoming decades, given the complex response in drought[31] and wildfires[32–35] to anthropogenic activity and global warming. Overall, our study calls for adaptation and/or mitigation strategies for this compound drought-fire-dust hazard, which is likely to become more frequent and severe with ongoing environmental change.

The uncertainty of our study mainly derives from the quality of the currently analyzed satellite data, especially retrieval difficulties. First, transported dust provides inevitable uncertainty for quantifying the intensity and duration of post-fire dust emissions, particularly over the African savannahs that are close to dry-land dust hotspots. Although we focus on coarse-mode dust optical depth as the metric for dust abundance to minimize the impacts of transported, smaller-sized dust particles on our results (see Methods), the retrieval of coarse-mode dust optical depth involves errors too[36,37]. A sensitivity test that addresses possibly non-local–originated high DODs suggests that transported dust may cause an overestimation of post-fire dust duration by 0–3 days (10^{th} – 90^{th} percentiles of all pixels from both regions) and maximum post-fire DOD by 0-7% in North Africa (**Supplementary Fig. 2**) and Australia (**Supplementary Fig. 3**). Second, deposited combustion ash from the burned vegetation could be lifted by strong winds along with mineral dust. Ash (typically 0 – 50 mm thick above surface) consists of mineral materials and charred organic components with a wide range of particle size, shape, and optical properties that partially overlap with dust[38]; therefore, the currently identified post-fire dust events, especially those shortly after burning, may contain a mixture of co-emitted dust and deposited ash. Here we perform a qualitative test that assumes pure dust emission only occurs after the first day of post-fire high DOD. This test confirms similar peak intensity of post-fire pure dust emissions versus potential dust-ash-mixture emissions (**Supplementary Fig. 4**). Nevertheless, a dust-ash-mixture storm can cause similar socioeconomic and health problems as a pure dust storm. With development of higher-quality satellite and ground observations, especially the hyperspectral and mineralogical information of dust and ash emitted from specific geographic locations, we will continue to quantify regional and global post-fire dust emissions. Based on this post-fire dust emission inventory, future observational and modeling studies should characterize the dynamical and optical properties of post-fire dust emissions, quantify their climatic impacts, and compare with regular dust emissions from dry lands.

Acknowledgements

This research is supported by Peking University School of Physics (Y.Y.), NASA grant number NNH19ZDA001N-HMA (P.G.), and the Earth Surface Mineral Dust Source Investigation (EMIT), a NASA Earth Ventures-Instrument (EVI-4) Mission (P.G.). The authors thank Dr. John Dunne for helpful comments on the early version of this paper. We thank the MODIS, MISR, AERONET, and CALIOP teams for providing data. We thank the Earth Surface Mineral Dust Source Investigation (EMIT) team, Dr. Jintai Lin, and Dr. Jiafu Mao for useful discussions. Computation is supported by High-performance Computing Platform of Peking University.

Author contributions

YY conceived the study, analysed the data, and wrote the manuscript with contribution from PG. PG retrieved MODIS DOD and FOD data from MODIS Deep Blue aerosol products.

Competing interests

The authors declare that they have no conflict of interest.

Figures

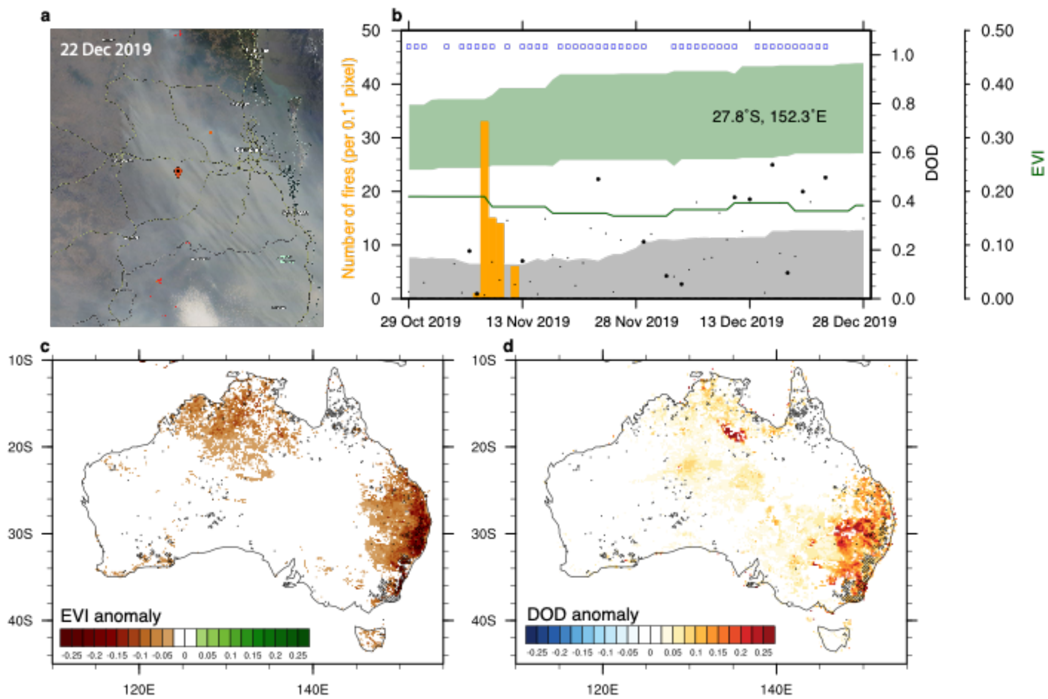

Figure 1 Extreme dust activity associated with vegetation disturbances caused by the 2019-2020 Australian bushfires. a. True color image of aerosol plumes originating from the active fires and burned areas in southeastern Australia on December 22, 2019, captured by the Moderate Resolution Imaging Spectroradiometer (MODIS) instrument onboard the Terra satellite that overpasses in local morning time. The red dots indicate active fires detected by MODIS onboard both the Terra and Aqua satellites, both day and night. **b.** Time series of active fire count (orange bars, referring to the left y-axis), enhanced vegetation index (EVI, green line, referring to rightmost y-axis), and daily maximum dust optical depth (DOD, black dots, referring to the inter right y-axis) within ±0.05˚ of 27.8˚S, 152.3˚E (location indicated in panel **a**). The blue squares indicate dates with abnormally dry soil (below long-term 10th percentile). The green and grey shadings represent the long-term 10th–90th percentiles in the daily EVI and DOD, respectively. The large and small black dots represent time series of DOD; large dots indicate situations with relatively small amount of biomass burning aerosols, represented by below-average coincident fine-mode optical depth (FOD). **c.** Anomaly in EVI during December 2019 to February 2020, compared to the long-term average during December to February of 2000–2020.

d. Anomaly in DOD during December 2019 to February 2020, compared to the long-term average during December to February of 2000–2020. In **c** and **d**, only the EVI anomalies and DOD anomalies more extreme than the long-term 10th–90th percentiles are shown in color. In **c** and **d**, the stitches and slashes indicate 0.1˚ pixels with more than 30 and 100, respectively, active fires during the December 2019 to February 2020 Australian bushfire season. Satellite image from NASA Earth Observatory. Figure created using NCL[39].

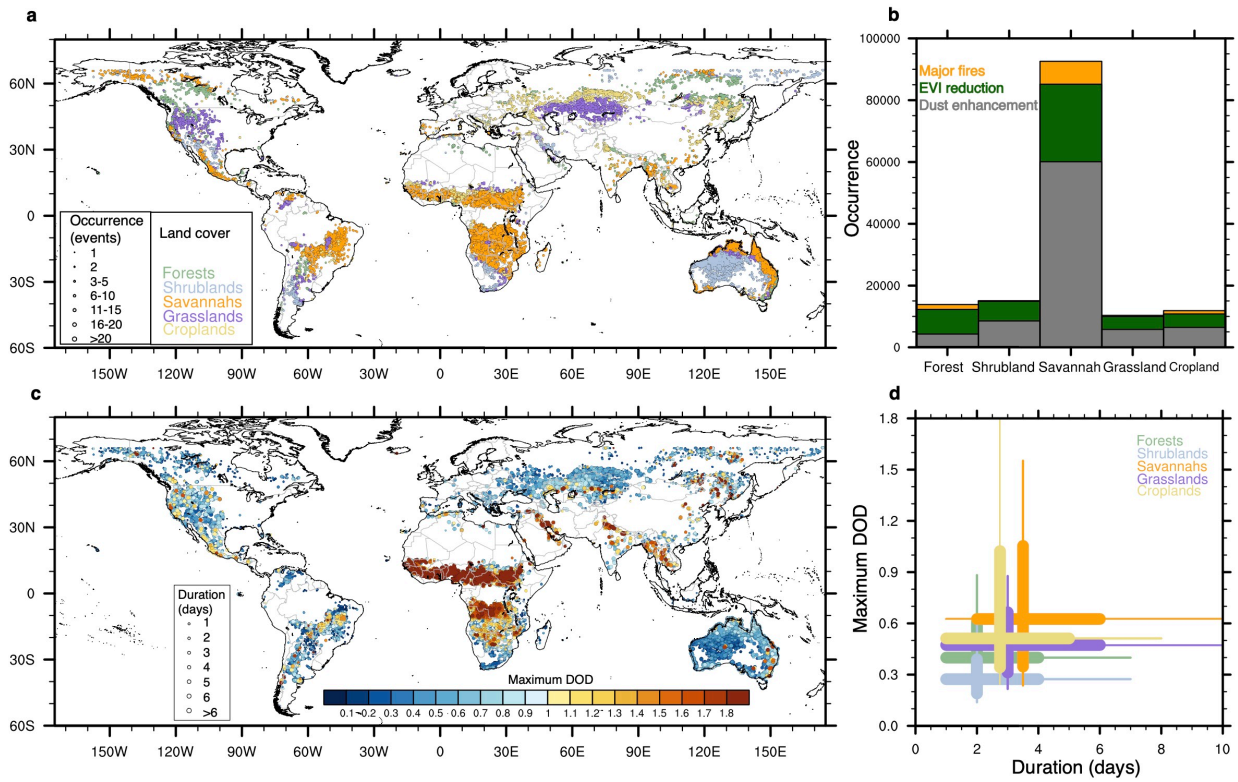

Figure 2 Global distribution of post-fire dust events. a. Occurrence of post-fire dust events during 2003–2020 indicated by the size of dots, with color representing the dominant land cover type. The land cover types are identified by the Moderate Resolution Imaging Spectroradiometer (MODIS) Terra+Aqua Combined Land Cover product following the International Geosphere Biosphere Programme (IGBP) scheme for the period 2003–2020. **b.** Total occurrence of large wildfire events (orange bars), significant Enhanced Vegetation Index (EVI) reduction (green bars), and dust emission (grey bars) by land cover type (see Methods). **c.** Maximum Dust Optical Depth (DOD, color of dots), representing the columnar dust loading associated with the most intensive post-fire dust emission, and mean duration (days, size of dots) of post-fire dust events. **d.** Boxplot (thin lines: 10th – 90th percentiles, thick lines: 25th – 75th percentiles, intersection:

median of both metrics) of maximum DOD and duration of post-fire dust events, by land cover type.

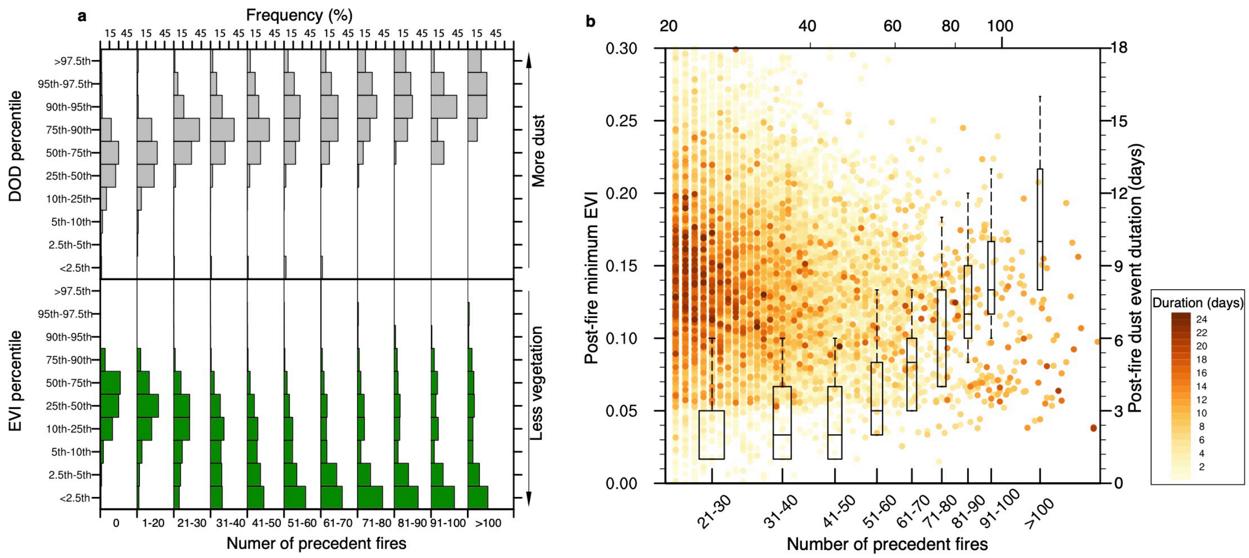

Figure 3 Severity of post-fire dust events regulated by the extent of precedent wildfires and vegetation disturbance. a. Probability distribution of post-fire, 30-day average (top) DOD and (bottom) EVI as a function of number of precedent fires. The probability distribution is represented by the frequency (%) of DOD and EVI below the long-term 2.5th percentile, between the 2.5th–5th, 5th–10th, 10th–25th, 25th–50th, 50th–75th, 75th–90th, 90th–95th, 95th–97.5th percentiles, and above the 97.5th percentile. **b.** Scatterplot of post-fire minimum EVI (referring to the left y-axis) and number of precedent fires. Each dot in **b** corresponds to a post-fire dust event, with the color representing the duration (days) of this event. The boxes in **b** indicate the 10th, 25th, 50th, 75th, and 90th percentiles of post-fire dust event duration (days, referring to the right y-axis) with precedent fires ranging between 21–30, 31–40, 41–50, 51–60, 61–70, 71–80, 81–90, 91–100, and above 100 during the burning period.

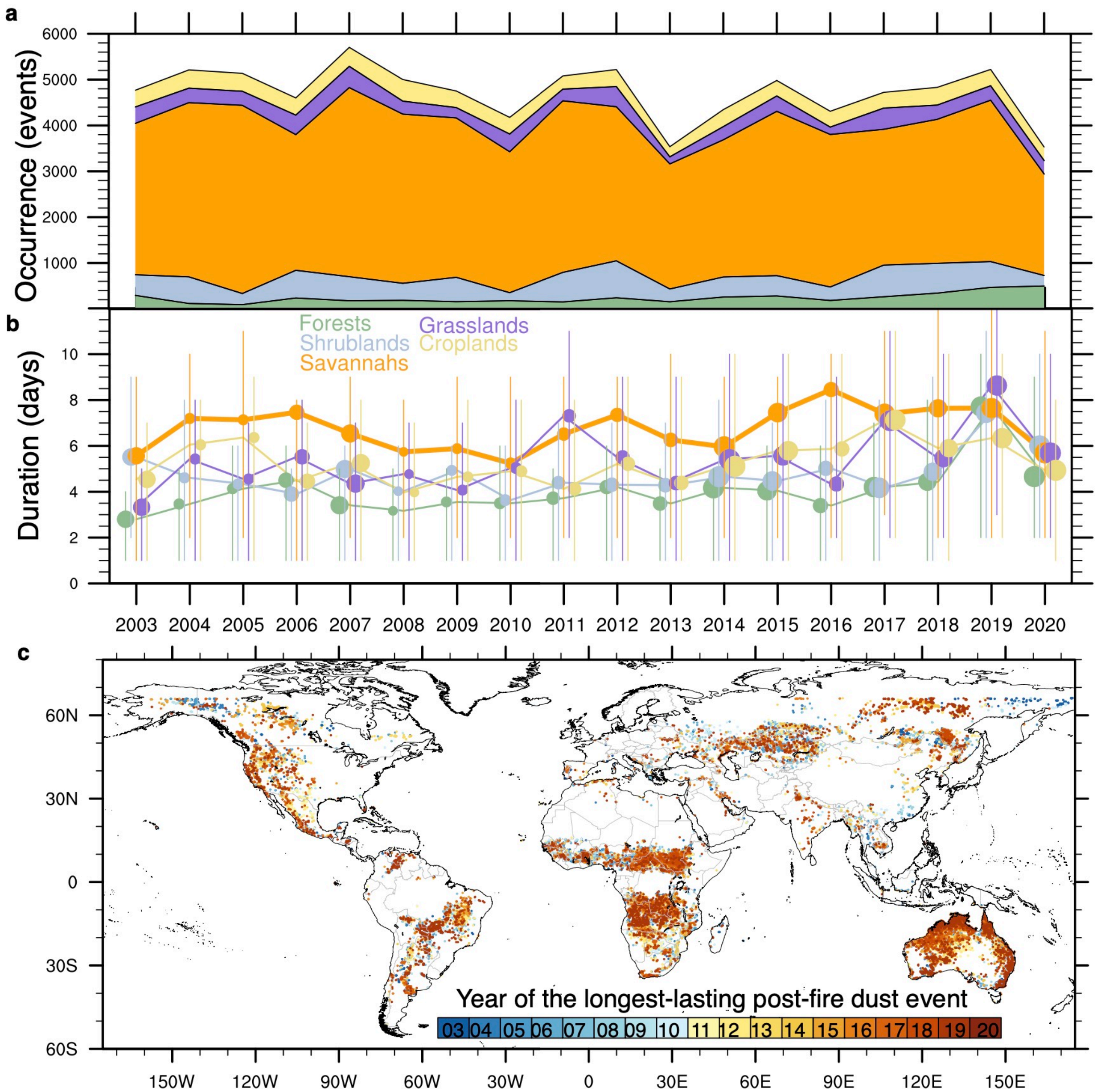

Figure 4 Observed evolution of the occurrence and duration of post-fire dust events during 2003–2020. a–b. Time series of the **a.** occurrence and **b.** mean duration (days) of post-fire dust events for each dominant land cover type during 2003–2020. In **b**., the sizes of dots are proportional to the average fire counts per large wildfire event for each land cover type and year. The thicknesses of the lines are proportional to the total occurrence of post-fire dust emission for each land cover type during 2003-2020. The vertical lines indicate the 10th to 90th percentiles of duration among all post-fire dust events for each land cover type and year. **c.** Year of the longest-duration post-fire dust event.

Methods

Satellite-based measurements of wildfire intensity

To assess the intensity of wildfires, we analyze the active fires reported by the Moderate Resolution Imaging Spectroradiometer (MODIS) onboard the polar-orbiting Terra and Aqua satellites. The collection 6.1 MODIS active fire product detects fires in 1-km pixels that burn at the time of overpass under relatively cloud-free conditions using a contextual algorithm. The detection algorithm uses native (i.e., unprojected swath) 4-, 11-, and 12-μm brightness temperatures derived from the corresponding1-km MODIS channels, and, for daytime observations, 0.65-, 0.86-, and 2.1-μm reflectance, aggregated to 1-km spatial resolution[40]. Daily wildfire intensity is examined here as the total active fire counts from both the day-time and night-time MODIS measurements.

The relatively coarse-resolution satellite measurements of active fires at about 1 km resolution may miss nearly half of the burned area in Africa detected by higher resolution satellite measurements (about 20 m resolution) in a given year[41]. The underrepresentation of small fires may lead to underestimation of small fire-induced dust emission.

Satellite-based measurements of dust and other aerosols

Dust Optical Depth (DOD) is a column-integration of extinction coefficient by mineral particles. The current study examines DOD from MODIS onboard the Terra and Aqua satellites and the non-spherical aerosol optical depth (nsAOD) from the Multiangle Imaging SpectroRadiometer (MISR) instrument[42] on Terra, during 2003-2020.

MODIS DOD represents the optical depth of absorbing, coarse-mode aerosols that are often dust over bare ground or sparsely vegetated regions. Following Pu et al. (2020)[43], daily MODIS DOD is retrieved from collection 6.1, level 2 MODIS Deep Blue aerosol products[44,45], including aerosol optical depth (AOD), single-scattering albedo (ω), and the Ångström exponent (α). All the daily variables are first interpolated to a $0.1^\circ \times 0.1^\circ$ grid using the algorithm described by Ginoux et al. (2010)[46]. To account for dust's absorption of solar radiation and separate dust from scattering aerosols, such as sea salt, we require the single-scattering albedo at 470 nm to be less than 0.99 for the retrieval of DOD. Based on the size distribution of dust towards the coarse range and to separate it from fine particles, DOD is retrieved as a continuous function of AOD and Ångström exponent:

$$DOD = AOD \times (0.98 - 0.5089\alpha + 0.051\alpha^2). \quad (1)$$

This retrieval of DOD is on the basis of Ångström exponent's sensitivity to particle size, with smaller values of Ångström exponent indicating larger particles[47], and the previously established relationship between Ångström exponent and fine-mode AOD[48]. Details about the retrieval process and estimated errors are summarized by Pu and Ginoux (2018)[37]. MODIS DOD products have been widely used for the identification and characterization of dust sources[21,49,50], as well as examination of variations in regional and global dustiness[37,43,51,52].

Following the recommendation from Baddock et al. (2016)[50] and previous applications of MODIS DOD[37,43,51,52], here we use DOD with a low-quality flag of QA = 1, under the assumptions that 1) dust sources are better detected using DOD with a low-quality flag, and 2) retrieved aerosol products are poorly flagged over dust source regions. For example, when the standard deviation of AOD between 10×10 pixels is greater than 0.18, the retrieval algorithm considers the scene as cloudy although intense dust plumes over dust sources could easily reach such value[50]. Indeed, the comparison with the Aerosol Robotic Network (AERONET) DOD shows drastically decreased sample size but minimally enhanced consistency for any land cover type after applying a higher quality flag (**Supplemental Figs. 5–6**).

The residual of total aerosol optical depth after subtracting DOD, namely fine-mode optical depth (FOD), represents the abundance of other aerosol species, which is primarily smoke aerosols over active fires. In short, DOD and FOD represent the atmospheric abundance of particles that are relatively coarse and fine, respectively, mainly reflecting dust and carbonaceous aerosols, over burned and active burning areas. Overall, the optimal spatial and temporal coverage of MODIS aerosol products with over 20 years' record warrant its application for studying the day-to-day variations and environmental drivers of global aerosol loads.

It should be noted that limited by the spatial resolution of MODIS aerosol products, our study is conducted at 0.1˚ latitude and longitude resolution (about 10 km near the equator), which may not be ideal for accurate representation of fire, dust, and environmental structures over complex landscapes.

Benefiting from its multiangle observations, MISR data can be used to directly retrieve AOD and particle properties[42]. In the current study, Version 23, Level 2, daily MISR 550-nm nonspherical AOD (nsAOD) at 4.4-km resolution[53] is compared with MODIS DOD. The MISR nonspherical AOD fraction is often referred to as "fraction of total AOD due to dust", as dust is the primary nonspherical aerosol particle in the atmosphere, especially over sparsely vegetated regions[54]. The MISR nsAOD has been used to examine variations in dustiness in North Africa and the Middle East[22,55–57]. Similar to our use of MODIS DOD with a low-quality flag, here we analyze the raw MISR nsAOD retrieval without quality filtering. MISR nsAOD data is also interpolated to a 0.1˚ × 0.1˚ grid using the algorithm described by Ginoux et al. (2010)[46]. Due to its relatively narrow swath of ~380 km, MISR samples the study region about every 2-16 days. The sparse sampling of MISR limits its application in understanding day-to-day variations of aerosols, such as in our current study; but MISR's capability at distinguishing dust particles from other aerosol species provides useful benchmark for evaluating other satellite-based approximate measurements of dust abundance. The correlation between temporally (both onboard the Terra satellite) and spatially (within 0.1˚ pixels) collocated MISR nsAOD and MODIS DOD measurements during 2019 to 2020 suggests a generally high consistency between the two measurements of dust mass loading (**Supplementary Fig. 7**). Correlation exceeding 0.7 is widely seen over the identified hotspot regions for post-fire dust emission (e.g. in **Figure 2**), such as tropical savannahs in Africa, South America, and northern and eastern Australia, shrublands in western Australia, grasslands and croplands in central Asia, and various landscapes in western North America (**Supplementary Fig. 7**), ensuring the reliability of MODIS DOD in the current analysis.

The Version 3, level 2 (cloud screened and quality assured), sub-daily AERONET coarse-mode AOD (DOD) and fine-mode AOD (FOD) at 500 nm obtained from the 205 sun photometers across the globe[58] and retrieved by the Spectral Deconvolution Algorithm (SDA) [59] are analyzed here to evaluate the accuracy of spatially and temporally collocated MODIS DOD and FOD, especially for various land cover types. Here a "collocated observation" is identified when there is available MODIS DOD and FOD over the 0.1˚ grid covering the AERONET site within ± 0.5

hour of the corresponding AERONET site observation. This definition results in a total of 64,390 collocated observations between AERONET and MODIS. The comparison shows acceptable consistency between MODIS and AERONET in both DOD (**Supplementary Fig. 5**) and FOD (**Supplementary Fig. 8**) across the major landscapes. Highest correlation and lowest root-mean square error (RMSE) between MODIS and AERONET DOD is seen over forests and savannahs, respectively (**Supplementary Fig. 5**). Highest correlation and lowest RMSE between MODIS and AERONET FOD are both seen over savannahs (**Supplementary Fig. 8**). Higher accuracy of MODIS DOD and FOD is particularly present for high DOD and FOD (**Supplementary Figs. 5, 8**).

Total attenuated backscatter and depolarization ratio at 532 nm, as well as aerosol subtype information from the Cloud-Aerosol Lidar with Orthogonal Polarization (CALIOP) Version 4.20 (V4) Level 2 aerosol products are analyzed to confirm episodic dust emission from post-fire landscapes in eastern Australian during the 2019–2020 bushfire season. The spaceborne lidar instruments, such as CALIOP aboard the Cloud Aerosol Lidar and Infrared Pathfinder Satellite Observation (CALIPSO) spacecraft[60], are able to provide vertical structure of aerosol and clouds. Despite CALIOP's limited spatial coverage (with a diameter of 70 m on Earth surface), the vertical distribution of aerosol abundance (reflected by total attenuated backscatter), aerosol shape (reflected by depolarization ratio, with a typical value of 0.2–0.3 for dust[61]), and aerosol subtypes (identified from altitude, location, surface type, estimated particulate depolarization ratio, integrated attenuated backscatter[62]) is particularly useful for identifying post-fire dust emission during selected events. Data for four nighttime overpasses on November 5, 2019, December 22, 2019, January 4, 2020, and January 22, 2020 are shown in **Extended Data Fig. 2**. These overpasses capture near-surface dust-smoke mixtures during active burning and pure dust after burning over the burned land in eastern Australia.

Satellite-based measurements of vegetation cover

Collection 6, MODIS Enhanced Vegetation Index (EVI) derived from atmospherically corrected reflectance in the red, near-infrared, and blue wavebands[63] is analyzed here for vegetation disturbances caused by wildfires. EVI and another vegetation index, the Normalized Difference Vegetation Index (NDVI), effectively characterize the global range of vegetation states and processes and have been successfully applied in various ecosystem, climate, and natural resources management studies[64,65]. Compared with NDVI, EVI minimizes canopy-soil variations and improves sensitivity over dense vegetation conditions. The VI's use a MODIS-specific compositing method based on product quality assurance metrics to remove low quality pixels. From the remaining good quality VI values, a constrained view angle approach then selects a pixel to represent the compositing period (from the two highest NDVI values it selects the pixel that is closest-to-nadir). Benefiting from the MODIS sensors aboard both Terra and Aqua satellites, here we analyze 16-day EVI composite eight days apart from both satellites, thereby obtaining a higher temporal resolution (8-day) product by combining both data records. Corresponding to the spatial resolution of analyzed aerosol data, the original 1-km EVI data is also interpolated to a $0.1^\circ \times 0.1^\circ$ grid using the algorithm described by Ginoux et al. (2010)[46].

Identification of dust emission after wildfires

The identification of post-fire dust events follows these steps: (1) We screen the daily 0.1° active fire count data to identify the location and time of the occurrence of large fires, namely more than 20 fires in consecutive seven days. Each location-time combination is defined as a large wildfire event. We choose 20 fires as the threshold for identifying large fires because of the minor change in the probability distributions of EVI and DOD after the occurrence of 1-20 fires during the antecedent burning week (**Figure 3a**). (2) Among these large wildfire events, we identify those with significant EVI reduction, i.e. any 8-day EVI that falls below the 10^{th} percentile of the long-term spread, during the subsequent 60 days after the end of burning. The long-term spread for a specific 0.1° pixel on a specific date of year is obtained by aggregating all 16-day EVI measurements from both MODIS-Terra and MODIS-Aqua within ±15 days of that date for that pixel during 2003-2020. (3) Among those large wildfire events that trigger significant EVI reduction, we then examine DOD and FOD measurements during the 60 days after the end of burning. A day with significant DOD increase, i.e., exceeding the 90^{th} percentile of long-term spread, from either morning or afternoon measurements and concurrent moderate-to-low FOD, i.e. below the 50^{th} percentile of long-term spread, from both the morning and afternoon measurements is defined as a post-fire dust emission day. The reason for excluding high FOD situations is to minimize contamination of flying ash and smoke aerosols over active fires on the DOD signal, as flying ash and smoke aerosols are mostly smaller particles compared with dust[66,67]. The long-term spread of DOD and FOD for a specific date of year and 0.1˚ pixel are aggregated from both MODIS-Terra and MODIS-Aqua within ±15 days of that date for that pixel during 2003-2020. The duration of a post-fire dust event is defined as the total number of post-fire dust emission days within 60 days of the end of burning. The maximum DOD of a post-fire dust event is defined as the maximum DOD among the post-fire dust emission days.

Note that the identification of post-fire dust events depends on the thresholds for significant EVI reduction and DOD increase. Among the analyzed 151,727 large fire events (52% of all week-pixel combinations that experienced at least one active fire), 91% and 78% are followed by any 8-day EVI falling below long-term 10th percentile and 5th percentile, respectively, during the subsequent 60 days; 54% and 37% are followed by any daily DOD reaching long-term 90th (with EVI below 10th percentile) and 95th (with EVI below 5th percentile) percentiles, respectively, during the subsequent 60 days.

Statistics of post-fire dust events for different land cover types

Number of large wildfire events, those with significant EVI reduction, and with post-fire dust emission events are reported for different land cover types, along with the distribution of the duration and maximum DOD of post-fire dust emissions. The land cover data is obtained from the collection 6 MODIS Terra+Aqua Combined Land Cover product[68]. We examine the primary land cover scheme that identifies 17 classes defined by the International Geosphere-Biosphere Programme (IGBP), including 11 natural vegetation classes, three human-altered classes, and three non-vegetated classes. The yearly land cover fraction data for the 17 classes originally at 0.05˚ latitude and longitude are first regridded to the same 0.1˚ grid as the aerosol data, following Ginoux et al. (2010). All global 0.1˚ pixels are then grouped to five dominant land cover types, namely forests (Evergreen needleleaf forests, Evergreen broadleaf forests, Deciduous needleleaf forests, Deciduous broadleaf forests, and mixed forests), shrublands (closed and open shrublands), savannahs (woody savannahs and savannahs), grasslands, and croplands (croplands and cropland/natural vegetation mosaics), using the 18-year average land cover fractions. Note that the uncertainty of the MODIS land cover data, such as the unrealistic savannahs in the boreal region (**Figure 2a**), may complicate the land cover-specific interpretation of current results[69].

Soil moisture and wind observations

To explore additional drivers of dust emission after wildfires, we analyze daily soil moisture at 0.1˚ spatial resolution from European Space Agency (ESA) Climate Change Initiative (CCI) soil moisture data[70] and hourly 10-m wind speed at 0.1˚ spatial resolution from European Centre for Medium-Range Weather Forecasts (ECMWF) Reanalysis v5 (ERA5)[71]. The ESA CCI soil moisture combines various single-sensor active and passive microwave soil moisture products into three harmonized products: a merged ACTIVE, a merged PASSIVE, and a COMBINED active + passive microwave product. Here we analyze the version 06.1 break-adjusted COMBINED daily soil moisture for the top layer[72]. This product involves several algorithm updates and represents the most accurate ESA CCI global soil moisture data from 1978-2020. ERA5 is the latest reanalysis from ECMWF covering the period of 1950 to near real time and assimilates various observations in the upper air and near surface. Regional evaluation of ERA5 hourly 10-m wind speed show vastly improved accuracy of ERA5 wind data compared with its older version ERA-Interim, but relatively large discrepancy with in situ observations remains over complex terrains[73,74]. In this study, we focus on daily maximum 10-m wind speed, which is directly related to dust emission[75] and obtained from the original hourly ERA5 reanalysis data. We obtain collocated daily soil moisture and daily maximum wind speed with observed dust at the nearest pixel of their original grid to the corresponding location of dust pixel.

Understanding post-fire dust emissions through examination of aerosols, EVI, soil moisture, and wind speed responses to large wildfires

To assess the temporal evolution of environmental responses to large wildfires, weekly averaged EVI, soil moisture, and aerosol, as well as weekly maximum wind speed, are examined in their probability distribution, i.e. the frequency of these variables falling below the long-term 2.5th percentile, between the 2.5th–5th, 5th–10th, 10th–25th, 25th–50th, 50th–75th, 75th–90th, 90th–95th, 95th–97.5th percentiles, and above the 97.5th percentile. For example, a frequency of certain variable falling below the long-term 2.5th percentile that exceeds 2.5% indicates a higher probability of extremely low value of this variable after the occurrence of large fires. The long-term percentiles of these variables for a specific week of year and 0.1˚ are aggregated from that week and ±1 week of the year for that pixel during 2003-2020.

To assess the response of aerosols, EVI, soil moisture, and wind speed to intensifying precedent fires, we examine 30-day average DOD, 30-day average and minimum EVI and 30-day minimum soil moisture, as well as and 30-day upper decile wind speed, either in their probability distribution or actual value, as a function of active fires during the antecedent week. In the probability distribution analysis, the long-term percentiles of each variable at 0.1° for a specific 30-day period of a year is constructed from 30-day running averages during ±30 days, respectively, of the center date of the year. Trend analysis of the occurrence and intensity of post-fire dust events, active fire accounts, and soil moisture involves the application of the Mann-Kendall nonparametric test for monotonic trend and Theil-Sen robust estimate of linear trend[76]. A monotonic upward (downward) trend means that the variable consistently increases (decreases) through time, but the trend may or may not be linear; thus the Mann-Kendall test is a more general approach than linear regression-based tests for identifying any upward or downward trend.

Data Availability

The datasets for conducting the analysis presented here are all publicly available, including: the MODIS Collection 6 Active Fire Detections (MCD14ML) acquired from NASA Fire Information for Research Management System (https://earthdata.nasa.gov/firms); the MODIS Deep Blue aerosol products acquired from the Level-1 and Atmosphere Archive and Distribution System (LAADS) Distributed Active Archive Center (DAAC) (https://ladsweb.modaps.eosdis.nasa.gov/); the MISR aerosol products acquired from the NASA Langley Research Center Atmospheric Science Data Center (https://l0dup05.larc.nasa.gov/cgi-bin/MISR/main.cgi); the AERONET coarse-mode aerosol optical depth data downloaded from https://aeronet.gsfc.nasa.gov; the ESACCI soil moisture data download from https://www.esa-soilmoisture-cci.org/node/238; the ERA-5 hourly climate data provided by ECMWF (https://www.ecmwf.int/en/forecasts/datasets/reanalysis-datasets/era5); the MODIS MCD12Q1v006 Landcover Type 1 product (https://lpdaac.usgs.gov/products/mcd12q1v006/); and the MODIS L3 EVI (MOD13C1 and MYD13C1) from DAAC (https://lpdaac.usgs.gov/products/mod13c1v006/). We generate a list of all identified dust emission cases following large fires available at https://doi.org/10.6084/m9.figshare.20648055[77].

Code Availability

The code to carry out the current analyses is available from the corresponding author upon request.

References

1. Bowman, D. M. J. S. *et al.* Fire in the earth system. *Science (80-.).* **324**, 481–484 (2009).
2. Bowman, D. M. J. S. *et al.* Human exposure and sensitivity to globally extreme wildfire events. *Nat. Ecol. Evol.* **1**, 1–6 (2017).
3. Hamilton, D. S. *et al.* Earth, Wind, Fire, and Pollution: Aerosol Nutrient Sources and Impacts on Ocean Biogeochemistry. *Ann. Rev. Mar. Sci.* **14**, 303–330 (2022).
4. Barkley, A. E. *et al.* African biomass burning is a substantial source of phosphorus deposition to the Amazon, Tropical Atlantic Ocean, and Southern Ocean. *Proc. Natl. Acad. Sci. U. S. A.* **116**, 16216–16221 (2019).
5. Schlosser, J. S. *et al.* Analysis of aerosol composition data for western United States wildfires between 2005 and 2015: Dust emissions, chloride depletion, and most enhanced aerosol constituents. *J. Geophys. Res. Atmos.* **122**, 8951–8966 (2017).
6. Wagner, R., Schepanski, K. & Klose, M. The Dust Emission Potential of Agricultural-Like Fires — Theoretical Estimates From Two Conceptually Different Dust Emission Parameterizations. *J. Geophys. Res. Atmos.* **126**, e2020JD034355 (2017).
7. Ichoku, C. *et al.* Biomass burning, land-cover change, and the hydrological cycle in Northern sub-Saharan Africa. *Environ. Res. Lett.* **11**, (2016).
8. Bowman, D. M. J. S. *et al.* Vegetation fires in the Anthropocene. *Nat. Rev. Earth Environ.* **1**, 500–515 (2020).
9. Duniway, M. C. *et al.* Wind erosion and dust from US drylands: a review of causes, consequences, and solutions in a changing world. *Ecosphere* **10**, (2019).
10. Okin, G. S., Gillette, D. A. & Herrick, J. E. Multi-scale controls on and consequences of aeolian processes in landscape change in arid and semi-arid environments. *J. Arid Environ.* **65**, 253–275 (2006).
11. Raupach, M. R. Drag and drag partition on rough surfaces. *Boundary-Layer Meteorol.* **60**, 375–395 (1992).

12. Webb, N. P. *et al.* Vegetation Canopy Gap Size and Height: Critical Indicators for Wind Erosion Monitoring and Management. *Rangel. Ecol. Manag.* **76**, 78–83 (2021).
13. Ellis, T. M., Bowman, D. M. J. S., Jain, P., Flannigan, M. D. & Williamson, G. J. Global increase in wildfire risk due to climate-driven declines in fuel moisture. *Glob. Chang. Biol.* **28**, 1544–1559 (2022).
14. Ravi, S. *et al.* Aeolian processes and the biosphere. *Rev. Geophys.* **49**, 1–45 (2011).
15. Wagenbrenner, N. S., Germino, M. J., Lamb, B. K., Robichaud, P. R. & Foltz, R. B. Wind erosion from a sagebrush steppe burned by wildfire: Measurements of PM10 and total horizontal sediment flux. *Aeolian Res.* **10**, 25–36 (2013).
16. Wagenbrenner, N. S. A large source of dust missing in Particulate Matter emission inventories? Wind erosion of post-fire landscapes. *Elem Sci Anth* **5**, (2017).
17. Jeanneau, A. C., Ostendorf, B. & Herrmann, T. Relative spatial differences in sediment transport in fire-affected agricultural landscapes: A field study. *Aeolian Res.* **39**, 13–22 (2019).
18. Deb, P. *et al.* Causes of the Widespread 2019–2020 Australian Bushfire Season. *Earth's Futur.* **8**, (2020).
19. Nogrady, B. & Nicky, B. the Climate Link To Australia's Fires. *Nature* **577**, (2020).
20. Yu, Y. & Ginoux, P. Assessing the contribution of the ENSO and MJO to Australian dust activity based on satellite- And ground-based observations. *Atmos. Chem. Phys.* **21**, 8511–8530 (2021).
21. Ginoux, P., Prospero, J. M., Gill, T. E., Hsu, N. C. & Zhao, M. Global-scale attribution of anthropogenic and natural dust sources and their emission rates based on MODIS Deep Blue aerosol products. *Rev. Geophys.* **50**, RG3005 (2012).
22. Yu, Y., Kalashnikova, O. V., Garay, M. J., Lee, H. & Notaro, M. Identification and Characterization of Dust Source Regions Across North Africa and the Middle East Using MISR Satellite Observations. *Geophys. Res. Lett.* **45**, 6690–6701 (2018).
23. Brianne, P., Rebecca, H. & David, L. The fate of biological soil crusts after fire: A meta-analysis. *Glob. Ecol. Conserv.* **24**, e01380 (2020).
24. Rodriguez-Caballero, E. *et al.* Global cycling and climate effects of aeolian dust controlled by biological soil crusts. *Nat. Geosci.* (2022). doi:10.1038/s41561-022-00942-1
25. Goudie, A. S. & Middleton, N. J. *Desert dust in the global system*. (Springer, 2006).

26. Ginoux, P. Atmospheric chemistry: Warming or cooling dust? *Nature Geoscience* **10**, 246–247 (2017).

27. DeMott, P. J. *et al.* Predicting global atmospheric ice nuclei distributions and their impacts on climate. *Proc. Natl. Acad. Sci.* **107**, 11217–11222 (2010).

28. Yu, H. *et al.* The fertilizing role of African dust in the Amazon rainforest: A first multiyear assessment based on data from Cloud-Aerosol Lidar and Infrared Pathfinder Satellite Observations. *Geophys. Res. Lett.* **42**, 1984–1991 (2015).

29. Tang, W. *et al.* Widespread phytoplankton blooms triggered by 2019–2020 Australian wildfires. *Nature* **597**, 370–375 (2021).

30. Sarangi, C. *et al.* Dust dominates high-altitude snow darkening and melt over high-mountain Asia. *Nat. Clim. Chang.* **10**, 1045–1051 (2020).

31. Cook, B. I. *et al.* Twenty-First Century Drought Projections in the CMIP6 Forcing Scenarios. *Earth's Futur.* **8**, 1–20 (2020).

32. Zheng, B. *et al.* Increasing forest fire emissions despite the decline in global burned area. *Sci. Adv.* **7**, (2021).

33. Abatzoglou, J. T. & Williams, A. P. Impact of anthropogenic climate change on wildfire across western US forests. *Proc. Natl. Acad. Sci. U. S. A.* **113**, 11770–11775 (2016).

34. Abram, N. J. *et al.* Connections of climate change and variability to large and extreme forest fires in southeast Australia. *Commun. Earth Environ.* **2**, (2021).

35. Yu, Y. *et al.* Machine learning–based observation-constrained projections reveal elevated global socioeconomic risks from wildfire. *Nat. Commun.* **13**, 1–11 (2022).

36. Pu, B. & Ginoux, P. How reliable are CMIP5 models in simulating dust optical depth ? *Atmos. Chem. Phys.* **18**, 12491–12510 (2018).

37. Pu, B. & Ginoux, P. Climatic factors contributing to long-term variations in surface fine dust concentration in the United States. *Atmos. Chem. Phys.* **18**, 4201–4215 (2018).

38. Bodí, M. B. *et al.* Wildland fire ash: Production, composition and eco-hydro-geomorphic effects. *Earth-Science Rev.* **130**, 103–127 (2014).

39. UCAR/NCAR/CISL/TDD. The NCAR Command Language (Version 6.6.2) [Software]. (2019). doi:http://dx.doi.org/10.5065/D6WD3XH5

40. Giglio, L., Schroeder, W. & Justice, C. O. The collection 6 MODIS active fire detection algorithm and fire products. *Remote Sens. Environ.* **178**, 31–41 (2016).

41. Ramo, R. *et al.* African burned area and fire carbon emissions are strongly impacted by small fires undetected by coarse resolution satellite data. *Proc. Natl. Acad. Sci. U. S. A.* **118**, 1–7 (2021).

42. Diner, D. J. *et al.* Multi-angle Imaging SpectroRadiometer (MISR) instrument description and experiment overview. in *IEEE Transactions on Geoscience and Remote Sensing* **36**, 1072–1087 (1998).

43. Pu, B. *et al.* Retrieving the global distribution of the threshold of wind erosion from satellite data and implementing it into the Geophysical Fluid Dynamics Laboratory land-atmosphere model (GFDL AM4.0/LM4.0). *Atmos. Chem. Phys.* **20**, 55–81 (2020).

44. Sayer, A. M., Hsu, N. C., Bettenhausen, C. & Jeong, M. J. Validation and uncertainty estimates for MODIS Collection 6 'deep Blue' aerosol data. *J. Geophys. Res. Atmos.* **118**, 7864–7872 (2013).

45. Hsu, N. C. *et al.* Enhanced Deep Blue aerosol retrieval algorithm: The second generation. *J. Geophys. Res. Atmos.* **118**, 9296–9315 (2013).

46. Ginoux, P., Garbuzov, D. & Hsu, N. C. Identification of anthropogenic and natural dust sources using moderate resolution imaging spectroradiometer (MODIS) deep blue level 2 data. *J. Geophys. Res.* **115**, 1–10 (2010).

47. Eck, T. F. *et al.* Wavelength dependence of the optical depth of biomass burning, urban, and desert dust aerosols. *J. Geophys. Res. Atmos.* **104**, 31333–31349 (1999).

48. Anderson, T. L. *et al.* Testing the MODIS satellite retrieval of aerosol fine-mode fraction. *J. Geophys. Res.* **110**, 1–16 (2005).

49. Baddock, M. C., Bullard, J. E. & Bryant, R. G. Dust source identification using MODIS: A comparison of techniques applied to the Lake Eyre Basin, Australia. *Remote Sens. Environ.* **113**, 1511–1528 (2009).

50. Baddock, M. C., Ginoux, P., Bullard, J. E. & Gill, T. E. Do MODIS-defined dust sources have a geomorphological signature? *Geophys. Res. Lett.* **43**, 2606–2613 (2016).

51. Pu, B. & Ginoux, P. Projection of American dustiness in the late 21st century due to climate change. *Sci. Rep.* **7**, 1–10 (2017).

52. Pu, B., Ginoux, P., Kapnick, S. B. & Yang, X. Seasonal Prediction Potential for Springtime Dustiness in the United States. *Geophys. Res. Lett.* **46**, 9163–9173 (2019).

53. Garay, M. J. *et al.* Introducing the 4.4 km spatial resolution Multi-Angle Imaging

SpectroRadiometer (MISR) aerosol product. *Atmos. Meas. Tech.* **13**, 593–628 (2020).

54. Kalashnikova, O. V., Kahn, R., Sokolik, I. N. & Li, W.-H. Ability of multiangle remote sensing observations to identify and distinguish mineral dust types: Optical models and retrievals of optically thick plumes. *J. Geophys. Res.* **110**, D18S14 (2005).
55. Yu, Y. *et al.* Assessing temporal and spatial variations in atmospheric dust over Saudi Arabia through satellite, radiometric, and station data. *J. Geophys. Res. Atmos.* **118**, 13253–13264 (2013).
56. Yu, Y., Notaro, M., Kalashnikova, O. V. & Garay, M. J. Climatology of summer Shamal wind in the Middle East. *J. Geophys. Res. Atmos.* **121**, 289–305 (2016).
57. Yu, Y. *et al.* Disproving the Bodélé Depression as the Primary Source of Dust Fertilizing the Amazon Rainforest. *Geophys. Res. Lett.* **47**, 1–12 (2020).
58. Giles, D. M. *et al.* Advancements in the Aerosol Robotic Network (AERONET) Version 3 database - Automated near-real-time quality control algorithm with improved cloud screening for Sun photometer aerosol optical depth (AOD) measurements. *Atmos. Meas. Tech.* **12**, 169–209 (2019).
59. O'Neill, N. T., Eck, T. F., Smirnov, A., Holben, B. N. & Thulasiraman, S. Spectral discrimination of coarse and fine mode optical depth. *J. Geophys. Res. Atmos.* **108**, 1–15 (2003).
60. Winker, D. M. *et al.* Overview of the CALIPSO mission and CALIOP data processing algorithms. *J. Atmos. Ocean. Technol.* **26**, 2310–2323 (2009).
61. Esselborn, M. *et al.* Spatial distribution and optical properties of Saharan dust observed by airborne high spectral resolution lidar during SAMUM 2006. *Tellus, Ser. B Chem. Phys. Meteorol.* **61**, 131–143 (2009).
62. Kim, M. H. *et al.* The CALIPSO version 4 automated aerosol classification and lidar ratio selection algorithm. *Atmos. Meas. Tech.* **11**, 6107–6135 (2018).
63. Didan, K., Munoz, A. B., Solano, R. & Huete, A. *MODIS Vegetation Index User 's Guide (Collection 6)*. (2015).
64. Seddon, A. W. R., Macias-Fauria, M., Long, P. R., Benz, D. & Willis, K. J. Sensitivity of global terrestrial ecosystems to climate variability. *Nature* **531**, 229–232 (2016).
65. Saleska, S. R. *et al.* Dry-season greening of Amazon forests. *Nature* **531**, E4–E5 (2016).
66. Remer, L. A., Kaufman, Y. J., Holben, B. N., Thompson, A. M. & McNamara, D.

Biomass burning aerosol size distribution and modeled optical properties. *J. Geophys. Res. Atmos.* **103**, 31879–31891 (1998).

67. Tegen, I. & Lacis, A. A. Modeling of particle size distribution and its influence on the radiative properties of mineral dust aerosol. *J. Geophys. Res. Atmos.* **101**, 19237–19244 (1996).
68. Friedl, M. A. & Sulla-Menashe, D. *User Guide to Collection 6 MODIS Land Cover (MCD12Q1 and MCD12C1) Product*. **6**, (2018).
69. Sulla-Menashe, D., Gray, J. M., Abercrombie, S. P. & Friedl, M. A. Hierarchical mapping of annual global land cover 2001 to present: The MODIS Collection 6 Land Cover product. *Remote Sens. Environ.* **222**, 183–194 (2019).
70. Dorigo, W. *et al.* ESA CCI Soil Moisture for improved Earth system understanding: State-of-the art and future directions. *Remote Sens. Environ.* **203**, 185–215 (2017).
71. Hersbach, H. *et al.* The ERA5 global reanalysis. *Q. J. R. Meteorol. Soc.* **146**, 1999–2049 (2020).
72. Preimesberger, W., Scanlon, T., Su, C.-H., Gruber, A. & Dorigo, W. Homogenization of Structural Breaks in the Global ESA CCI Soil Moisture Multisatellite Climate Data Record. *IEEE Trans. Geosci. Remote Sens.* **59**, 2845–2862 (2021).
73. Minola, L. *et al.* Near-surface mean and gust wind speeds in ERA5 across Sweden: towards an improved gust parametrization. *Clim. Dyn.* **55**, 887–907 (2020).
74. Molina, M. O., Gutiérrez, C. & Sánchez, E. Comparison of ERA5 surface wind speed climatologies over Europe with observations from the HadISD dataset. *Int. J. Climatol.* **41**, 4864–4878 (2021).
75. Klose, M. *et al.* Mineral dust cycle in the Multiscale Online Nonhydrostatic Atmosphere Chemistry model (MONARCH) version 2.0. *Geosci. Model Dev.* **14**, 6403–6444 (2021).
76. Mondal, A., Kundu, S. & Mukhopadhyay, A. Rainfall Trend Analysis By Mann-Kendall Test: a Case Study of North-Eastern Part of Cuttack District, Orissa. *Int. J. Geol. Earth Environ. Sci.* **2**, 2277–208170 (2012).
77. Yu, Y. & Ginoux, P. Dust emission following large wildfires. *Figshare* (2022). doi:10.6084/m9.figshare.20648055.v2